

***Declaration:***

*This is a non-peer reviewed preprint (EarthArXiv) version. The final peer-reviewed version will be available after acceptance which can be accessed through the "Peer-Reviewed Publication DOI" link.*

**Rayleigh wave H/V amplitude ratio measurement  
using multicomponent ambient noise cross-correlations,  
and its relationship to Vp/Vs**

**Authors** : Ajay Malkoti<sup>1,2</sup>,  
Arjun Datta<sup>1,3\*</sup>,  
Shravan M. Hanasoge<sup>1</sup>

**Email** : \*arjun.datta@tifr.res.in

**Affiliation:** : <sup>1</sup>Department of Astronomy and Astrophysics,  
Tata Institute of Fundamental Research  
Homi Bhabha Road, Colaba, Mumbai 400005, India.  
: <sup>2</sup>*Presently at* CSIR-National Geophysical Research Institute,  
Hyderabad-500007, India  
: <sup>3</sup>*Presently at* Department of Earth and Climate Science,  
Indian Institute of Science Education and Research Pune,  
Dr. Homi Bhabha Road, Pashan, Pune 411008, India.

**Abstract**

The promise of passive seismology has increasingly been realized in recent years. Given the expense in installing and maintaining seismic station networks, it is important to extract as much information from the measurements as possible. In this context, the ellipticity or  $H/V$  amplitude ratio of Rayleigh waves can prove to be a valuable observable in ambient noise seismology due to its complimentary sensitivity to subsurface structure, compared to phase and group-velocity dispersion, as well as its potential for constraining  $V_P$  structure in addition to  $V_S$ . However, the suitability of the Rayleigh  $H/V$  ratio in noise-based studies depends on the accurate interpretation of measurements made on multi-component ambient-noise cross-correlations. We present a synthetic study that critically examines measurements commonly interpreted as the Rayleigh wave  $H/V$  ratio, under realistic scenarios of spatially distributed and non-uniform noise sources. Using the surface wave terms of Green's function in a laterally homogeneous medium, we rigorously model multi-component cross-correlations

for arbitrary noise-source distributions and extract from them standard estimates of the H/V ratio. Variation of these measurements as a function of  $V_p$  is studied empirically, by brute-force simulation. We find that the measurements depart significantly from the theoretical Rayleigh wave H/V for the medium in question, when noise sources are strongly directional or anisotropic. Love waves, if present in the cross correlations, also have the potential to significantly bias interpretation. Accurate interpretation of the H/V ratio measurement thus rests on carefully modelling these effects. However, the sensitivity to  $V_p$  structure is comparable to that of the classic Rayleigh wave H/V. We also propose a new measurement for cross-correlations that has slightly greater sensitivity to  $V_p$ . Finally, uncertainty analysis on synthetic tests suggests that simplistic interpretations of Rayleigh wave ellipticity are only effective (in resolving  $V_p$  structure) when the Love-wave contamination is negligible and measurement uncertainties are less than 10%.

Keywords: *Seismic noise, Seismic interferometry, Surface waves and free oscillations, Crustal imaging*

## 1 Introduction

Ambient noise cross-correlation is a popular technique used to study shallow Earth structure using observations of the ambient seismic field on Earth, commonly known as ‘ambient noise’. The widespread use of this technique over the last 15 years has been largely based on the theoretical principle that the cross-correlation of a diffuse and equipartitioned noise wavefield recorded at two receivers, is proportional to the causal and anticausal far-field Green’s function between them (Shapiro & Campillo, 2004; Snieder, 2004; Weaver & Lobkis, 2004). Heavy pre-processing of raw noise records and averaging of cross-correlations over sufficiently long times is adopted in practice (Bensen et al., 2007), to recover ‘empirical Green’s functions’. Even so, most applications recover only the surface-wave Green’s function because the global noise field is dominated by ocean microseisms (Ardhuin et al., 2011, 2015) which originate near the Earth’s surface and strongly excite seismic surface waves. Since the traditional surface-wave measurements of phase and group velocity dispersion are dominantly sensitive to shear-wave velocity ( $V_S$ ), ambient noise has primarily been used to study Earth’s  $V_S$  structure.

By contrast, recovery of P-wave velocities ( $V_p$ ) from ambient noise is more challenging. Body waves, including P-waves, are hard to detect in ambient noise cross-correlations (due to weak excitation by shallow sources producing the noise wavefield) and the number of studies that have succeeded in doing so are limited (e.g. Roux et al., 2005; Poli et al., 2012; Nakata et al., 2015, 2016; Liu et al., 2016; Saygin et al., 2017; Pedersen & Colombi, 2018; Wang et al., 2018). An alternative candidate approach for studying  $V_p$ , that does not require P-wave observations, is to make use of the Rayleigh wave ellipticity or H/V ratio.

Rayleigh wave H/V ratio (ratio of horizontal to vertical component amplitudes) is an unconventional surface-wave observable compared to the more widely used dispersion measurement. It has a shallower sensitivity to Earth structure, specifically the elastic parameters  $V_P$ ,  $V_S$  and density  $\rho$  (Tanimoto & Rivera, 2008; Muir & Tsai, 2017), and has been used in joint-inversions with phase velocity dispersion, to constrain both  $V_P$  and  $V_S$  (Lin et al., 2012, 2014). We are therefore interested in its potential for  $V_P$  imaging.

Historically, Rayleigh wave H/V has seen limited use as a seismological imaging tool, perhaps due to the difficulty in obtaining stable measurements (Ferreira & Woodhouse, 2007; Tanimoto & Rivera, 2008; Ringler et al., 2019). However, this has changed in recent years, with many researchers exploring its potential for probing upper-crustal structure, both in the context of classical earthquake seismology (Berbellini et al., 2016; Lin et al., 2012; Ringler et al., 2019; Yano et al., 2009) and ambient noise interferometry (Berg et al., 2018; Li et al., 2016; Lin et al., 2014; Muir & Tsai, 2017; Roux, 2009; Savage et al., 2013). In the latter case, horizontal-to-vertical amplitude ratios obtained from multi-component cross-correlations are interpreted as the Rayleigh-wave H/V ratio, because the correlation signals are believed to contain Rayleigh waves (identified by their elliptical polarization) travelling between pairs of stations. By way of disambiguation, we note that such measurements differ from the ‘H/V spectral ratio’ obtained from single-station noise records (Nakamura, 1989; Fäh et al., 2001) which may or may not be related to the Rayleigh wave H/V ratio (Bonnefoy-Claudet et al., 2006). In this paper, we are concerned only with the Rayleigh-wave H/V ratio.

With the maturing of the field of ambient-noise seismology, it is important to rigorously analyse the estimation of Rayleigh H/V ratios from seismic-noise data. The theoretical conditions for Green’s-function retrieval from noise correlations are often not satisfied in reality due to non-stationary and heterogeneously distributed noise sources (Stehly et al., 2006; Ardhuin et al., 2011, 2015; Ermert et al., 2017). Consequently, a significant number of studies have warned of inaccurate empirical Green’s functions that suffer from artefacts, as well as traveltimes and amplitude errors (Fichtner, 2014; Froment et al., 2010; Halliday & Curtis, 2008; Kimman & Trampert, 2010; Tsai, 2009, 2011; Yao & van der Hilst, 2009). It is therefore to be expected that Rayleigh wave H/V ratios, which depend on relative amplitudes between components, are also similarly affected. Xu & Mikesell (2017) explicitly confirmed biases in the noise-correlation-derived Rayleigh wave Green’s tensor, that arise from heterogeneous noise sources.

In this study we do not invoke Green’s function interpretations for noise-correlation signals; instead we model these signals rigorously for arbitrary spatial distributions of noise sources (Section 2). To our knowledge, no previous study that models cross-correlations in this manner has analysed the Rayleigh H/V measurement in detail. Through a series of synthetic tests, we quantify the dependence of this measurement on the anisotropy of

noise-source distribution, as well as on model  $V_P$ , to assess its utility in practice (Sections 3 and 4). Measurement uncertainties, estimated by adding Gaussian noise to synthetic cross-correlation waveforms, shed light on the resolving power with respect to  $V_P$ .

## 2 Methodology

### 2.1 Modelling theory

In this section, we describe how the multi-component CCs are synthesized and used to obtain measurements of H/V ratio. In the frequency domain, ensemble-averaged CCs under the assumption of spatially uncorrelated noise sources (Tromp et al., 2010; Sager et al., 2018; Fichtner & Tsai, 2019) take the general form:

$$C_{pq}(\mathbf{x}_\alpha, \mathbf{x}_\beta) = \int_{\oplus} d\xi G_{pi}^*(\mathbf{x}_\alpha, \xi) G_{qj}(\mathbf{x}_\beta, \xi) S_{ij}(\xi) \quad (1)$$

where  $\mathbf{x}_\alpha, \mathbf{x}_\beta$  are the receiver locations;  $G_{mn}$  are elements of the Green's tensor satisfying  $\mathcal{L} G_{mn}(\mathbf{x}, \xi) = \delta_{mn} \delta(\mathbf{x} - \xi)$  for a wave operator  $\mathcal{L}$  (subscripts  $m$  and  $n$  correspond to the component of motion at the receiver location  $\mathbf{x}$ , and the direction of the point force at the source location  $\xi$ , respectively);  $S_{ij}$  is the power spectral density (PSD) matrix of the noise sources, and the integral is over the Earth volume  $\oplus$ . In this study we simplify eq. (1) with a few assumptions. First, noise sources are assumed to be present only on the Earth's surface (e.g. Tromp et al., 2010), so the volume integral reduces to a surface integral over its upper boundary  $\Omega$ , and we can restrict our modelling to just the surface-wave part of Green's function. Next, we consider noise sources acting in a single direction only, so the source PSD matrix reduces to a scalar term  $S$ . We further assume that the frequency characteristics of  $S$  are spatially invariant (Hanasoge, 2013, 2014; Datta et al., 2019), so that the spatial and frequency dependence of  $S$  may be separated, i.e.  $S(\xi, \omega) = P(\omega) \sigma(\xi)$ . These three simplifications lead to the expression:

$$C_{pq}(\mathbf{x}_\alpha, \mathbf{x}_\beta; \omega) = P(\omega) \int_{\Omega} d\xi G_{pi}^*(\mathbf{x}_\alpha, \xi, \omega) G_{qj}(\mathbf{x}_\beta, \xi, \omega) \sigma(\xi) \quad (2)$$

The evaluation of eq. (2) is still a three-step process in general, based on the invocation of source-receiver reciprocity at one of the receiver locations (Tromp et al., 2010; Sager et al., 2018). However in the specific case of working with a single receiver pair, as in this synthetic study, it is most efficient to invoke reciprocity at both receiver locations (Hanasoge, 2014; Xu et al., 2019), thereby rewriting eq. (2) as

$$C_{pq}(\mathbf{x}_\alpha, \mathbf{x}_\beta, \omega) = \int_{\Omega} d\xi G_{ip}^*(\xi, \mathbf{x}_\alpha, \omega) G_{iq}(\xi, \mathbf{x}_\beta, \omega) P(\omega) \sigma(\xi) \quad (3)$$

Hence  $C_{pq}$  is computed as follows. First, we obtain the  $i$ -component of impulse response in the entire horizontal domain for sources placed at the receiver locations and acting in the  $p$  and  $q$  directions. Next, we spatially integrate the product of the two responses (after complex conjugating one of them), weighted by the source mask  $\sigma$ .

This formulation is completely general with regard to the type of Earth model considered and the manner in which the Green's functions are obtained (e.g. analytically or numerically). In our implementation, we work with 1-D, vertically stratified media for which surface-wave terms of the elastodynamic Green's tensor are semi-analytically computable in 2-D as well as 3-D.

## 2.2 Computation of the Green's function

In our forward modelling scheme, we use a source direction  $i$  set to either  $z$  (vertical direction) or  $x$  (radial direction, see Figure 1), which corresponds to excitation of Rayleigh waves alone, or both Rayleigh and Love waves, respectively. In laterally homogeneous media, the Rayleigh- and Love-wave terms of Green's function for a point source at  $x = y = 0$ ,  $z = h$ , are (Aki & Richards, 2002, Sec 7.4):

$$\mathbf{G}^{RAY}(x, y, z) = \sum_n \frac{1}{8cUI_1} \begin{bmatrix} r_1(h)r_1(z)\frac{x^2}{r^2} & r_1(h)r_1(z)\frac{xy}{r^2} & -ir_2(h)r_1(z)\frac{x}{r} \\ r_1(h)r_1(z)\frac{xy}{r^2} & r_1(h)r_1(z)\frac{y^2}{r^2} & -ir_2(h)r_1(z)\frac{y}{r} \\ ir_1(h)r_2(z)\frac{x}{r} & ir_1(h)r_2(z)\frac{y}{r} & r_2(h)r_2(z) \end{bmatrix} \times H_0^{(1)}(k_n r) \quad (4)$$

$$\mathbf{G}^{LOV}(x, y, z) = \sum_n \frac{l_1(h)l_1(z)}{8cUI_1} \begin{bmatrix} \frac{y^2}{r^2} & \frac{-xy}{r^2} & 0 \\ \frac{-xy}{r^2} & \frac{x^2}{r^2} & 0 \\ 0 & 0 & 0 \end{bmatrix} \times H_0^{(1)}(k_n r) \quad (5)$$

Here  $r_1, r_2$  (Rayleigh) and  $l_1$  (Love) are displacement eigenfunctions and we write  $r = \sqrt{x^2 + y^2}$ . All symbols follow the Aki & Richards (2002) convention. However, our expressions are different inasmuch as we use cartesian rather than cylindrical coordinates (we work with a Cartesian grid  $\xi$ ), and abandon the far-field approximation. The Hankel function of the first kind,  $H_0^{(1)}$ , is used instead of its asymptotic form, because the implementation of (3) necessitates computation of Green's function at distances comparable to or shorter than a wavelength (see Sec. 3.1).

To evaluate expressions (4) and (5), we solve the surface-wave eigenvalue problem by the method of Gombert & Masters (1988), as in Datta et al. (2017); Datta (2018). This gives phase velocity  $c$ , group velocity  $U$  and the eigenfunctions  $r_1, r_2$  and  $l_1$ , which are numerically integrated to obtain the energy integral  $I_1$ . Since we only need to evaluate  $\mathbf{G}$  for sources and receivers on the surface, we use  $h = z = 0$ .

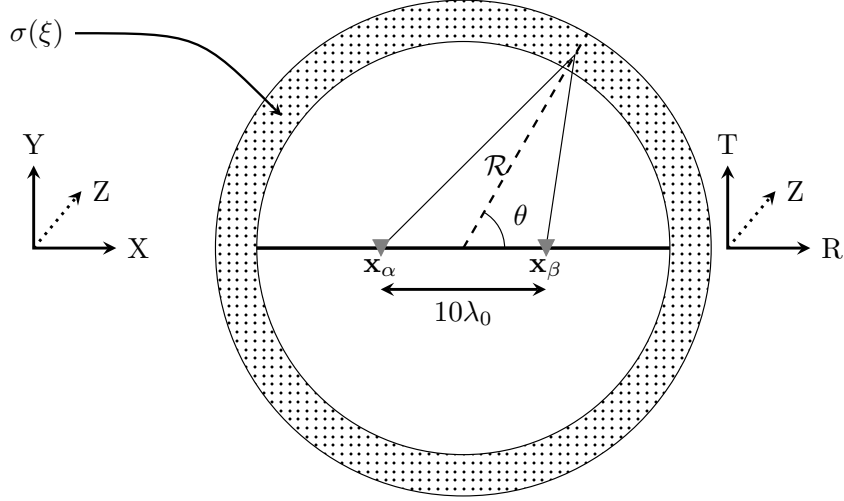


Figure 1: Schematic showing arrangement of sources (dots) and receivers (inverted triangles) in the modelling domain  $\Omega$ . The coordinate axes R, T and Z, represent the radial, transverse and vertical directions respectively, for the receiver pair.

### 2.3 H/V ratio measurement

Rayleigh waves are polarized in the radial-vertical (R-Z) plane and their H/V ratio refers to the ratio  $\eta$  of the radial to vertical displacement amplitudes (e.g. Maupin, 2017). In a laterally homogeneous medium,  $\eta$  is easily obtained from the displacement eigenfunctions evaluated at the surface. By definition,

$$\eta(\omega) = \frac{r_1(z=0, \omega)}{r_2(z=0, \omega)}. \quad (6)$$

Equivalently, one may write

$$\eta = \frac{|G_{RZ}|}{|G_{ZZ}|} = \frac{|G_{RR}|}{|G_{ZR}|}. \quad (7)$$

The equivalence between eqs.(7) and (6) is seen from eq. (4), when the  $x, y$  axes are oriented along the radial and transverse directions respectively (e.g. Fig. 1). Since the second index in the Green's tensor  $G_{ij}$  refers to the source orientation, eq. (7) asserts that  $\eta$  is a medium property, independent of whether the source (point-force) is vertical or radial.

In the case of ambient noise CCs, most studies define the Rayleigh H/V ratio analogously to eq. (7) using the corresponding elements of the cross-correlation tensor:  $C_{RR}, C_{ZZ}, C_{ZR}, C_{RZ}$ . Since CCs are usually obtained after some pre-processing of raw noise records (e.g. Bensen et al., 2007), it is important that any normalization is applied uniformly across different components, so as to preserve the relative amplitudes between them (Lin et al., 2014; Muir & Tsai, 2017). In this study, we work only with synthetics so there is no processing, but we note that all analogies with real-data scenarios require that multi-component seismic records be processed collectively rather than independently.

If equivalence between cross-correlations and Green's function holds, the two CC measurements,  $\Gamma^R$  and  $\Gamma^Z$ , correspond to virtual sources oriented radially and vertically respectively, as indicated by their superscripts:

$$\begin{aligned}\Gamma^R &= \frac{f(C_{RR})}{f(C_{ZR})} \sim \eta \\ \Gamma^Z &= \frac{f(C_{RZ})}{f(C_{ZZ})} \sim \eta.\end{aligned}\tag{8}$$

Here, the function  $f$  on the right hand side represents operations applied on the CCs to obtain robust measurements. In this study, we 1) Determine the envelope of the cross-correlation signal, 2) Pick its maximum value on the causal and anti-causal branches, 3) Average the two values thus obtained.

On the other hand, since cross-correlations and Green's functions are not necessarily equivalent (e.g. when source illumination is anisotropic), we define a third measurement  $\Gamma$ , which does not afford an interpretation in terms of a virtual source. It is the ratio between  $C_{RR}$  and  $C_{ZZ}$ . From the forward model (2), we have:

$$\begin{aligned}C_{RR} &\propto \int G_{RZ}^* G_{RZ} \\ C_{ZZ} &\propto \int G_{ZZ}^* G_{ZZ}\end{aligned}\tag{9}$$

when  $i = Z$  in (2), or

$$\begin{aligned}C_{RR} &\propto \int G_{RR}^* G_{RR} \\ C_{ZZ} &\propto \int G_{ZR}^* G_{ZR}\end{aligned}\tag{10}$$

when  $i = R$ . Therefore it is expected that  $C_{RR}/C_{ZZ}$  is proportional to  $G_{RZ}^2/G_{ZZ}^2$  when noise sources are vertical, and to  $G_{RR}^2/G_{ZR}^2$  when sources act along the radial direction for a given receiver pair. In general, given the definition (7), we estimate that  $\Gamma$  is related to the square of the classical Rayleigh wave H/V:

$$\Gamma = \frac{f(C_{RR})}{f(C_{ZZ})} \sim \eta^2.\tag{11}$$

### 3 Simulations

We perform a suite of simulations designed to empirically assess the sensitivity of H/V measurements to  $V_p$  structure, as well as gross geometrical features of the noise-source

distribution  $\sigma$ . These are the two quantities which we vary in our forward modelling, while other parameters are held fixed. As explained in the previous section, our modelling scheme entails a 1-D, depth-dependent Earth model  $M(z)$  in which the Green's functions are computed, and a 2-D horizontal domain  $\Omega(x, y)$  on which the sources are distributed (the Earth model is implicitly uniform throughout  $\Omega$ ). Here we first describe the fixed parameters, pertaining to  $\Omega$ , and then the model variations, which involve both  $M$  and  $\Omega$ .

### 3.1 Fixed parameters

Rayleigh wave H/V ratio is a frequency-dependent quantity but for the sake of simplicity, (most) results presented in this paper correspond to a single frequency,  $f_0 = 0.1$  Hz. This value (10 s period) is chosen because it lies in between the primary and secondary microseism peaks at  $\sim 7$  and 15 s (Peterson, 1993; Ardhuin et al., 2015). This choice of frequency dictates nearly all other choices relating to the simulation geometry. We model the PSD of the noise sources,  $P(\omega)$ , with a narrow-band Gaussian centered at  $f_0 = 0.1$  Hz (see Fig. 3f). The corresponding wavelength,  $\lambda_0$ , is used to fix the uniform grid spacing  $\Delta h \leq \lambda_0/4$  and separation between receivers,  $|\mathbf{x}_\alpha - \mathbf{x}_\beta| \geq 10\lambda_0$ , well above the typical requirement of three wavelengths (Bensen et al., 2007; Luo et al., 2015). The size of the domain  $\Omega$  is chosen to be at least twice the receiver separation in both directions, i.e.,  $[x_{\min}, x_{\max}, y_{\min}, y_{\max}] = 20\lambda_0 \times [-1, 1, -1, 1]$ .

We have  $\lambda_0 \approx 32.8$  km for Earth model  $M_0$  (see section 3.2), which leads to the values  $\Delta h = 5$  km,  $\mathbf{x}_\alpha = (-162.5 \text{ km}, 0)$ ,  $\mathbf{x}_\beta = (162.5 \text{ km}, 0)$  and  $\Omega = \{-600 \text{ km} < x < 600 \text{ km}, -600 \text{ km} < y < 600 \text{ km}\}$ . Note that the receivers are kept off-grid, since our implementation (3) places sources at their locations, and Green's functions (4), (5) blow up at the source. Finally, we use a temporal sampling interval of 1 s and generate a time series of length 400 s.

### 3.2 Models used

The 1-D Earth model used for the simulations is derived from the global CRUST2.0 model (Bassin, 2000), by extracting it at the location ( $60^\circ$  N,  $60^\circ$  E) where the crust is relatively thick at 50 km. We call this model  $M_0$ . Simulations are performed for 21 variants of this model, which differ only in their  $V_p$  values — a relative perturbation in the range  $-10\%$  to  $+10\%$  is applied uniformly at all depths to the model  $V_p$ .

Each Earth model  $M$  is used in conjunction with a particular model for the source distribution  $\sigma$  over the domain  $\Omega$ . We use different classes of  $\sigma$ . *Uniform distribution* where the sources have uniform strength everywhere in the domain; *Ring distribution* where sources are present at some distance ( $\mathcal{R}$ ) from the center of domain within a strip of width  $d\mathcal{R}$  (Fig. 1), and *Arc distribution* where sources are confined to an arc, with given  $\mathcal{R}$  and  $d\mathcal{R}$ , oriented at some angle to the receiver pair. We use  $\mathcal{R} = 500$  km and  $d\mathcal{R} = 40$  km for ring and



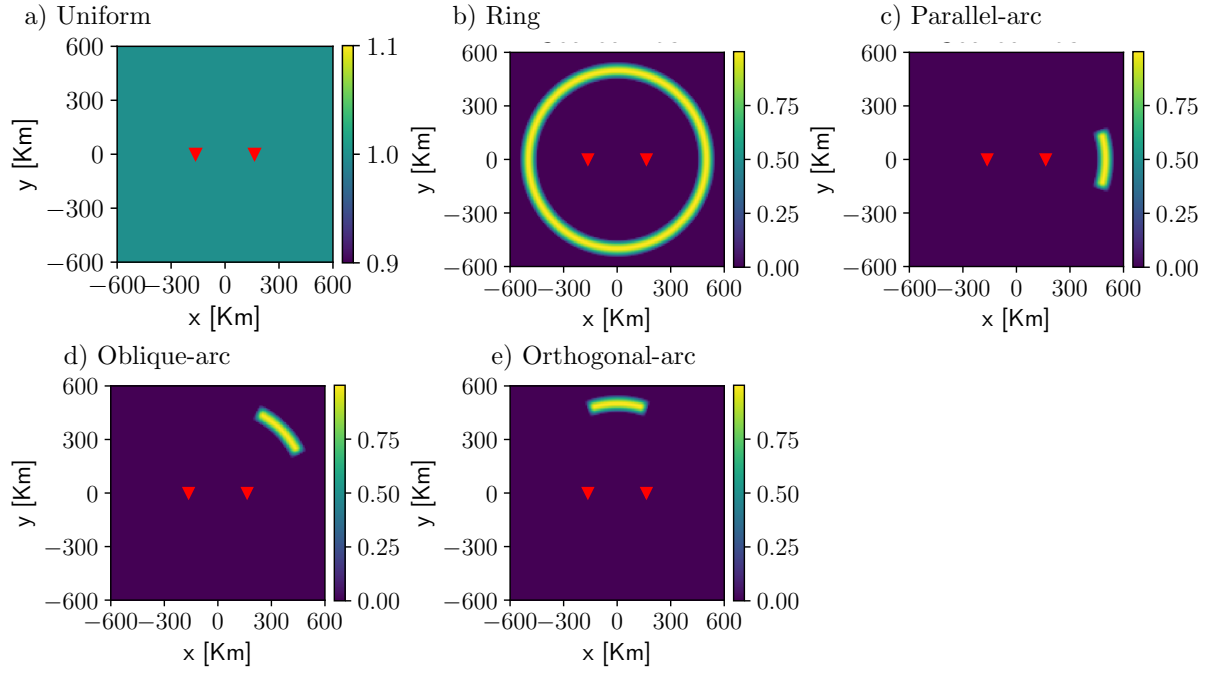


Figure 2: Different noise source distributions as defined in the text and identified here by the individual plot titles. The red triangles mark the receiver locations.

arc distributions. Three arc distributions are implemented to cover the range of possible scenarios of source directionality with respect to the receiver pair: *parallel* ( $\theta = -15^\circ$  to  $15^\circ$ ), *oblique* ( $\theta = 30^\circ$  to  $60^\circ$ ), and *orthogonal* ( $\theta = 75^\circ$  to  $105^\circ$ ). The arcs have uniform source strength in the aforementioned ranges for  $\theta$ , but are cosine tapered to zero over an additional  $5^\circ$  at both ends.

The five source-distribution models utilized for the simulations are shown in Fig. 2.

## 4 Analysis and results

We start by examining the CC obtained for each of the noise-source distributions in Earth model  $M_0$ . These are shown in Figure 3 for vertically oriented sources and fundamental-mode Rayleigh waves ( $n = 0$  in equation (4)). The effect of anisotropic source distributions is readily observed on the amplitude (in positive and negative branches,  $A^+$ ,  $A^-$ ) as well as arrival time ( $T_{CC}$ ) of signals in the CC. Uniform and ring distributions show  $A^+ = A^-$  and nearly the same arrival times as for Rayleigh waves ( $T_R$ ) with one of the receivers acting as a virtual source. In contrast, the arc-type distributions have  $A^+ \neq A^-$  and  $T_{CC} = T_R$  holds only for the parallel-arc configuration. These observations are well understood in terms of stationary and non-stationary phase sources (e.g. Xu & Mikesell, 2017). Figure 8 in the Supplementary Information shows the corresponding results for horizontal sources.

Next, we look at various H/V measurements obtained for all our Earth models with varying  $V_p$ . Simulations are performed separately for vertical and horizontal sources. The

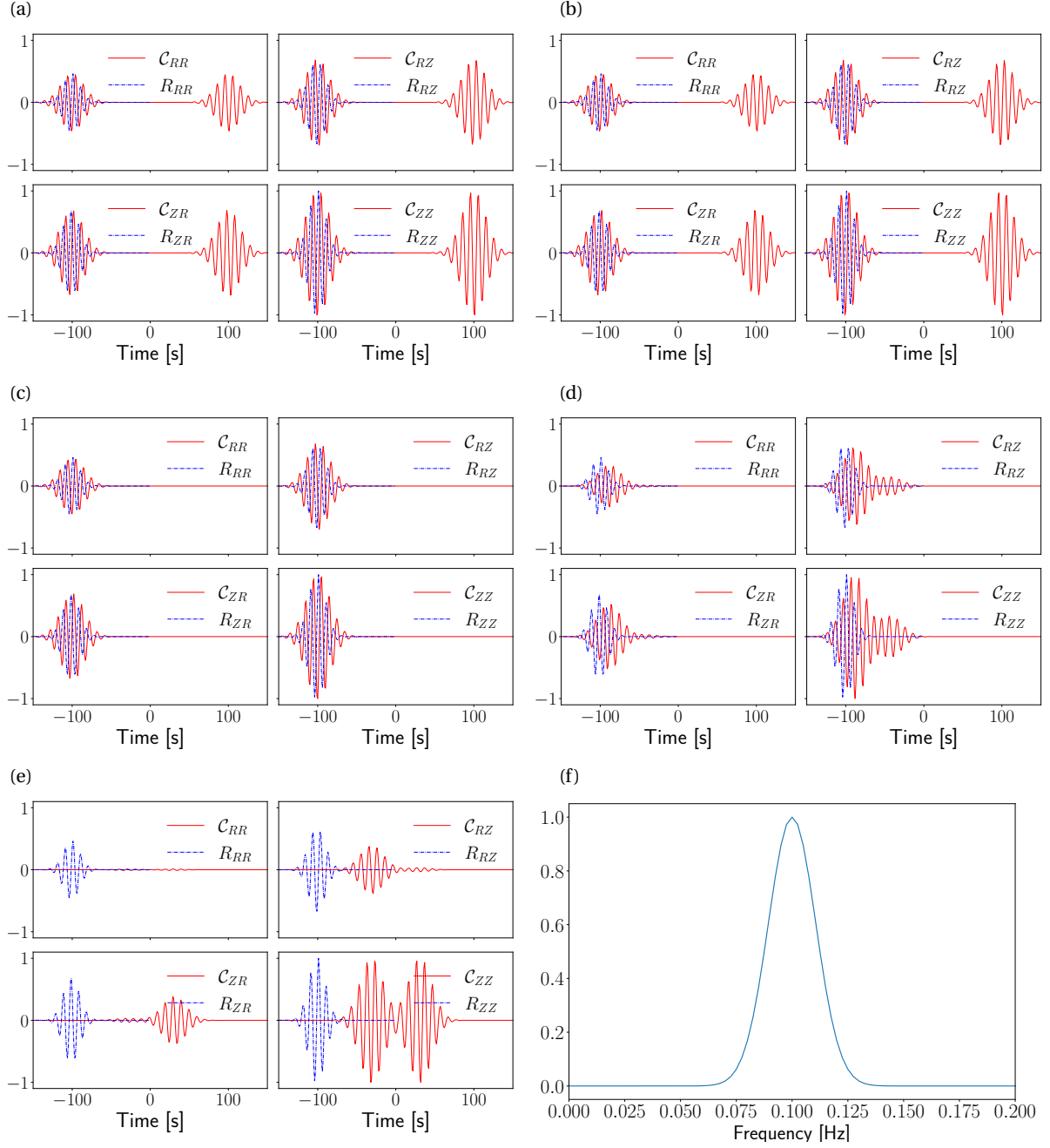


Figure 3: Panels (a)-(e) show the synthetic CCs generated for the corresponding source distributions in Fig. 2, with ‘zR’ source excitation. Each panel contains four plots for the four components (clockwise from top left)  $C_{RR}$ ,  $C_{RZ}$ ,  $C_{ZZ}$  and  $C_{ZR}$ . The corresponding Rayleigh wave from  $x_\alpha$  to  $x_\beta$  has also been presented for comparison. The amplitudes are normalized with respect to the maximum within a panel. (f)  $P(\omega)$  for the noise sources, centred at 0.1 Hz.

former act in the  $z$ -direction and excite Rayleigh waves only, hence are denoted ‘zR’; the latter act in the  $x$ -direction and excite both Love and Rayleigh waves, hence are denoted ‘xRL’. Figure 4 shows  $H/V$  as a function of  $V_p$ , for different noise source distributions, and for zR as well as xRL simulations. We find that for zR,  $H/V$  measurements for the uniform and ring distributions have an excellent match with the theoretical Rayleigh wave  $H/V$  ratio, i.e.  $\Gamma^R = \Gamma^Z \approx \eta$  and  $\Gamma \approx \eta^2$ . On the question of sensitivity to  $V_p$ , this implies that  $\Gamma$  offers better resolution than  $\Gamma^R$  or  $\Gamma^Z$  — the ‘dynamic range’ of  $\eta$ , i.e. the difference between its maximum and minimum values over the range of Earth models used, is  $\eta_{DR} \approx 0.085$  whereas for  $\eta^2$  it is slightly higher,  $\eta^2_{DR} \approx 0.104$  (also apparent from the slopes of the graphs). For xRL, there is a systematic offset between the  $\Gamma$ -curves and the  $\eta$ -curves in case of the uniform distribution, while the ring distribution case shows reasonable agreement.

Moving on to the anisotropic (arc-type) noise source distributions, there is reasonable agreement with theory only in the zR, parallel-arc case. All other cases exhibit a breakdown of the equivalence relations between the CC-derived  $H/V$  and the theoretical Rayleigh wave  $H/V$ . For xRL, the highly deviant measurements in the oblique- and orthogonal-arc scenarios are expected, due to strong Love wave components along the radial direction between the receivers. In the parallel-arc case, the discrepancies are much lower but still significant, because they are comparable to the dynamic range of the theoretical  $H/V$ . This observation is noteworthy because many studies deal with the issue of anisotropic noise sources, by only incorporating receiver pairs that are aligned with the dominant source illumination direction, which is often constrained only in a qualitative sense. Figure 4(f) suggests that very tight constraints on noise sources-receiver pair alignment are required to avoid Love wave contamination in CC-derived  $H/V$  measurements. {As a side note/interestingly}, the condition  $\Gamma^R = \Gamma^Z$  holds up for all cases except the orthogonal-arc in zR, and hold for all cases except the oblique- and orthogonal-arcs for xRL.

We also analysed the sensitivity of  $H/V$  to perturbations at different depths, by perturbing each layer in the model separately, rather than whole-model perturbations as described above. These tests, shown in Figures 10-12, confirm the well-known shallow sensitivity of Rayleigh wave  $H/V$ . Model perturbations in the first layer, down to 17 km depth, dominate the impact on  $H/V$ , with deeper perturbations having little impact except at longer periods.

Finally, inclusion of higher modes in our analyses did not provide additional insight, due to the order-of-magnitude weaker excitation of higher modes for the types of sources and model considered.

## 4.1 Measurements with added synthetic noise

The excitation of ambient noise in the Earth is a stochastic process and, when working with real data, seismologists typically use an ‘ensemble average’ over a large number of

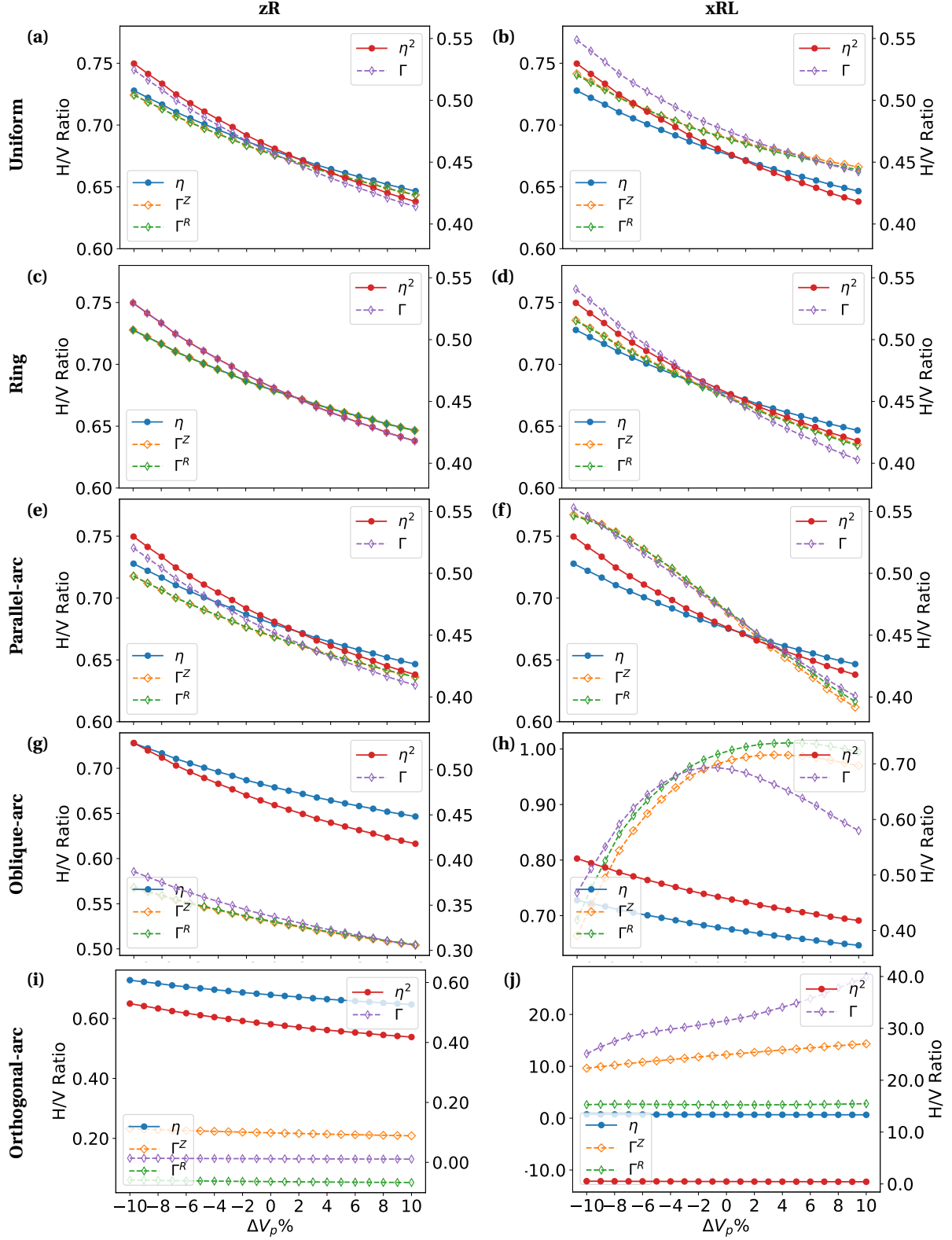


Figure 4: H/V ratio as a function of model  $V_p$ , for different noise source distributions along rows (labels on the left-hand side) and the two different source excitations along columns (labels at the top). In each plot, the CC-derived measurements (lines with diamonds) are compared with the theoretical Rayleigh wave H/V for the medium (lines with circles), the latter being the same in all plots. Note that we have used separate y-axes for different curves, shown on the left- and right-hand sides of each plot. The legend boxes attached to these two axes identify the curves associated.

cross-correlations (by stacking CC waveforms over various durations of time, from days or weeks to several months) as the basic measurement from which useful inferences can be derived. Therefore in practice, there is always a ‘realization noise’ associated with ambient noise CC-derived measurements. This constitutes a random noise level in ambient noise data, which is always present. Thus, no matter how accurate the source or structure models are, predicted and observed cross correlations will always be different because of realization noise. In this study, one of our aims is to assess the sensitivity of H/V measurements to  $V_p$ , and so we compare it to estimates of noise levels in the data.

To this end, we compute synthetic estimates of measurement uncertainty in the present section by adding random noise to our synthetic CC waveforms. The magnitudes of uncertainties, compared with the dynamic range of the measurements (over the range of  $V_p$  values considered) sheds light on the usefulness of these measurements in practice. We note that numerical simulations with added random noise have been used in the literature to simulate ensemble cross-correlations (Cupillard & Capdeville, 2010).

We obtain noisy synthetic waveforms  $\tilde{s}(t)$ , by adding noise  $N(t)$ , of chosen strength, to the noise-free signal  $s(t)$ , as

$$\tilde{s}(t) = s(t) + \frac{\alpha k}{100} N(t), \quad (12)$$

where  $\alpha$  is the desired signal to noise ratio and  $k$  is a scaling factor to bring the noise amplitudes to the signal level.  $N$  is computed in the frequency domain, using the power spectrum of the signal:

$$N(\omega) = P(\omega)\chi(\omega) \quad (13)$$

where  $P(\omega) = s^*(\omega)s(\omega)$ ,  $\chi(\omega) = [\mathcal{N}(0, 1) + j\mathcal{N}(0, 1)]/\sqrt{2}$  and  $\mathcal{N}(\mu, \sigma)$  represents a Gaussian random variable with mean,  $\mu$ , and standard deviation,  $\sigma$  (not to be confused with the source mask defined earlier).

H/V ratio calculations are performed for a given amount of noise (viz. 2%, 5% and 10%) and for each source distribution and Earth model, using all three H/V ratios, i.e. equations (8) and (11). The results are shown in Figure 5 (for the zR case; xRL case shown in Fig 9), with standard error estimated from 1000 realizations of added random noise.

As in the noise-free case, the mean trend of estimated H/V ratio in the presence of added noise closely follows the theoretical curves for homogeneous, ring and parallel-arc distributions. For the oblique-arc distribution there is a significant departure of mean trend from the theoretical curves containing a large error. For the orthogonal-arc distribution the H/V observation are completely erroneous. The uncertainty in estimated H/V ratios ( $\Gamma^R$ ,  $\Gamma^Z$ , and  $\Gamma$ ) in the presence of noise helps us evaluate the efficacy of measurements based on the thresholds given by  $\eta_{DR}$  for  $\Gamma^R$  and  $\Gamma^Z$ , and by  $\eta_{DR}^2$  for  $\Gamma$ . We infer two things from the

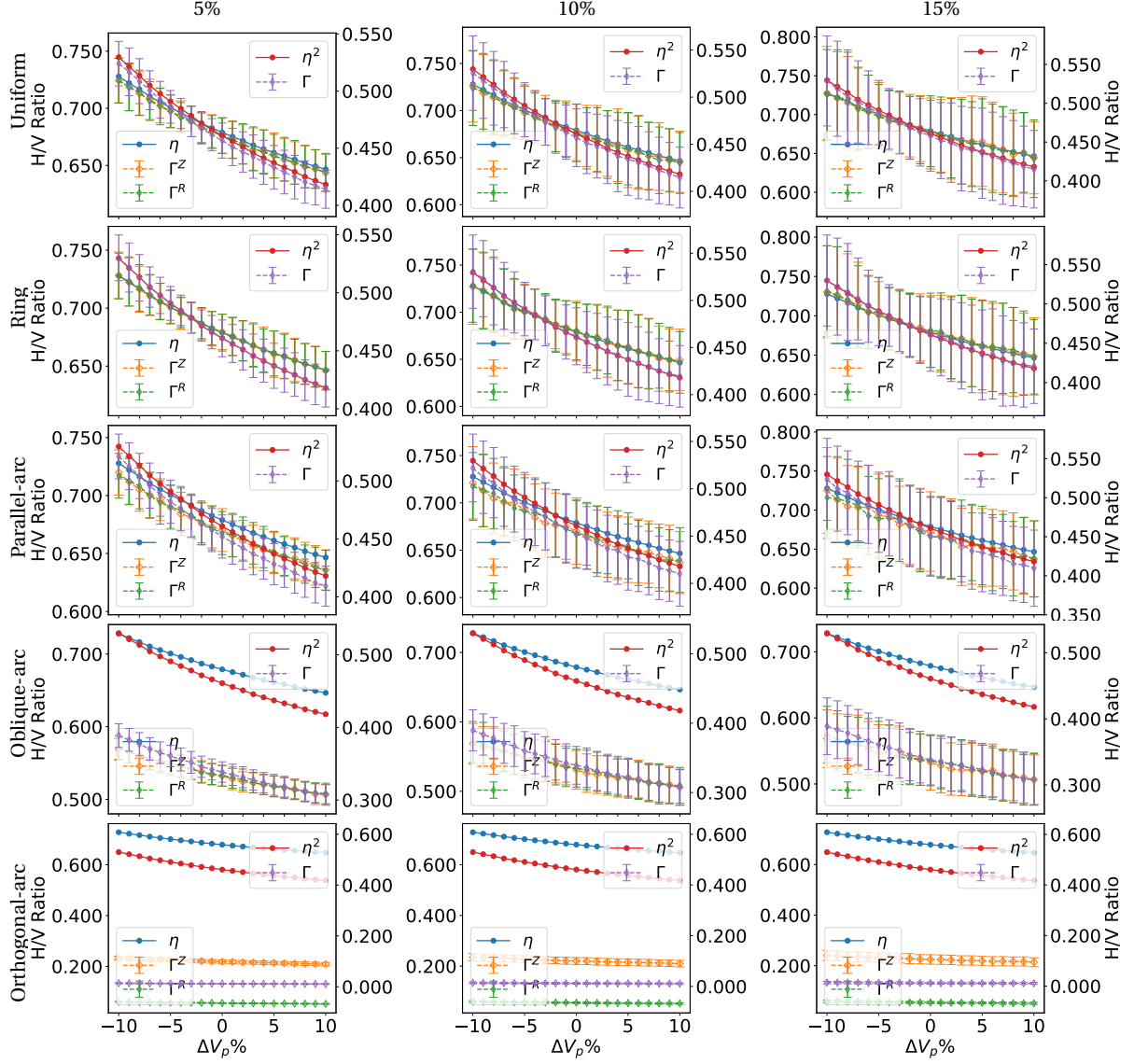


Figure 5: Similar to Fig. 4 but for measurements made with synthetic noise added to the CC, for zR source excitation. Noise levels vary across columns as indicated in the top panel, and rows correspond to source distributions as indicated on the extreme left.

observed values. First, meaningful measurements can only be made for up to 10% random Gaussian noise. Beyond this noise level, the uncertainties in CC-derived H/V ratios reach or exceed the  $\eta_{DR}$  or  $\eta^2_{DR}$  thresholds. Second, noise has a lower impact on  $\Gamma$  in comparison to  $\Gamma^R$  and  $\Gamma^Z$ , due to its larger dynamic range.

## 5 Discussion and conclusions

We have presented a synthetic study that critically examines measurements commonly used to estimate the Rayleigh-wave ellipticity or H/V ratio, from multi-component CCs of ambient noise recordings. In practice these measurements may be expected to be influenced by a variety of factors — anisotropic noise source illumination, interference from Love waves or higher-mode surface waves, and complicated wave propagation effects due to heterogeneous Earth structure. Our numerical study investigates some of these factors whilst simultaneously assessing the sensitivity of these measurements to  $V_P$  structure. It is based on (quasi) full-wave modelling of noise CCs in a 1-D elastic medium, and leads to the following conclusions:

1. Relative amplitudes between different components of the CC tensor, particularly those used to compute H/V, are biased by anisotropically distributed noise sources. Unless the pre-processing techniques are capable of satisfactorily mitigating the spatial variability of noise sources, this bias cannot be eliminated (note that we apply no additional processing in this synthetic study).
2. Love wave contributions, if present in the ambient noise field, produce a significant bias which is negligible only for highly favourable, and therefore likely unrealistic, distributions of noise sources.
3. H/V measurements do show sensitivity to  $V_P$ , but these may be easily undermined by data uncertainties on the order  $\sim 10\%$  or higher.
4. Sensitivity to  $V_P$  may be enhanced by using the measurement  $\Gamma = C_{RR}/C_{ZZ}$ , which recovers the square of the Rayleigh wave H/V ratio when noise sources are favourably distributed.

To deepen the understanding gained in this study, as well as to overcome the limitations of the EGF approach highlighted herein, we advocate constructing (finite-frequency) sensitivity kernels for  $\Gamma^R, \Gamma^Z, \Gamma$ , using the forward model (2). In particular, this will provide insight into the hitherto unexplored  $\Gamma$  measurement, which defies conventional interpretation in an EGF framework. In general, this will allow for all types of measurements to be used in practice without the biases inherent in the EGF approach.

The need for treating these measurements as independent observables, outside the EGF framework, is only amplified by consideration of 3-D structural effects, which we did not model in this study. We have shown the contamination of noise CC-derived H/V measurements due to features of the ambient noise source field alone. Additional contamination is expected from lateral variations in Earth structure, which can cause scattering and path bending, potentially tilting the particle polarization away from the R-Z plane. All of these complexities argue in favour of modelling cross-correlation rigorously (as in (2)) and using the same forward model to derive sensitivity kernels for any measurement of interest. These kernels will honour the measurement for what it is, minimising the danger of misinterpretation and leading to a better-posed, if more involved, inverse problem. Construction of such finite frequency sensitivity kernels is the subject of ongoing research.

## Acknowledgement

This work was funded by Shell India Markets Pvt.Ltd. A.D. acknowledges support from Shell contract PT75508 while at TIFR. We are grateful to the two anonymous reviewers whose comments helped to substantially improve this manuscript.

## References

- Aki, K. & Richards, P. G., 2002. *Quantitative seismology*, University Science Books.
- Ardhuin, F., Stutzmann, E., Schimmel, M., & Mangeney, A., 2011. Ocean wave sources of seismic noise, *Journal of Geophysical Research: Solid Earth*, **116**(C9), C09004.
- Ardhuin, F., Gualtieri, L., & Stutzmann, E., 2015. How ocean waves rock the Earth: Two mechanisms explain microseisms with periods 3 to 300 s, *Geophysical Research Letters*, **42**(3), 765–772.
- Bassin, C., 2000. The current limits of resolution for surface wave tomography in north america, *EOS Trans. AGU. 81: Fall Meet. Suppl., Abstract*.
- Bensen, G. D., Ritzwoller, M. H., Barmin, M. P., Levshin, A. L., Lin, F., Moschetti, M. P., Shapiro, N. M., & Yang, Y., 2007. Processing seismic ambient noise data to obtain reliable broadband surface wave dispersion measurements, *Geophysical Journal International*, **169**(3), 1239–1260.
- Berbellini, A., Morelli, A., & Ferreira, A. M. G., 2016. Ellipticity of Rayleigh waves in basin and hard-rock sites in Northern Italy, *Geophysical Journal International*, **206**(1), 395–407.



- Berg, E., Lin, F.-C., Allam, A., Qiu, H., Shen, W., & Ben-Zion, Y., 2018. Tomography of Southern California via Bayesian joint inversion of rayleigh wave ellipticity and phase velocity from ambient noise cross-correlations, *Journal of Geophysical Research: Solid Earth*, **123**(11), 9933–9949.
- Bonnefoy-Claudet, S., Cornou, C., Bard, P. Y., Cotton, F., Moczo, P., Kristek, J., & Fäh, D., 2006. H/V ratio: A tool for site effects evaluation. Results from 1-D noise simulations, *Geophysical Journal International*, **167**(2), 827–837.
- Cupillard, P. & Capdeville, Y., 2010. On the amplitude of surface waves obtained by noise correlation and the capability to recover the attenuation: a numerical approach, *Geophysical Journal International*, **181**(3), 1687–1700.
- Datta, A., 2018. SWRT: A package for semi-analytical solutions of surface wave propagation, including mode conversion, across transversely aligned vertical discontinuities, *Geoscientific Instrumentation, Methods and Data Systems*, **7**(1), 101–112.
- Datta, A., Priestley, K. F., Roecker, S., & Chapman, C. H., 2017. Surface wave mode coupling and the validity of the path average approximations in surface waveform inversions: an empirical assessment, *Geophysical Journal International*, **211**(2), 1099–1120.
- Datta, A., Hanasoge, S., & Goudswaard, J., 2019. Finite frequency inversion of cross-correlation amplitudes for ambient noise source directivity estimation, *Journal of Geophysical Research: Solid Earth*, **124**.
- Ermert, L., Sager, K., Afanasiev, M., Boehm, C., & Fichtner, A., 2017. Ambient Seismic Source Inversion in a Heterogeneous Earth: Theory and Application to the Earth's Hum, *Journal of Geophysical Research: Solid Earth*, **122**(11), 9184–9207.
- Ferreira, A. M. G. & Woodhouse, J. H., 2007. Observations of long period Rayleigh wave ellipticity, *Geophysical Journal International*, **169**(1), 161–169.
- Fichtner, A., 2014. Source and processing effects on noise correlations, *Geophysical Journal International*, **197**(3), 1527–1531.
- Fichtner, A. & Tsai, V. C., 2019. Theoretical Foundations of Noise Interferometry, in *Seismic Ambient Noise*, pp. 109–143, eds Nakata, N., Gualtieri, L., & Fichtner, A., Cambridge University Press, 1st edn.
- Froment, B., Campillo, M., Roux, P., Gouédard, P., Verdel, A., & Weaver, R. L., 2010. Estimation of the effect of nonisotropically distributed energy on the apparent arrival time in correlations, *GEOPHYSICS*, **75**(5), SA85–SA93, Publisher: Society of Exploration Geophysicists.

- Fäh, D., Kind, F., & Giardini, D., 2001. A theoretical investigation of average H/V ratios, *Geophysical Journal International*, **145**(2), 535–549.
- Gomberg, J. S. & Masters, T. G., 1988. Waveform modelling using locked-mode synthetic and differential seismograms: application to determination of the structure of Mexico, *Geophysical Journal International*, **94**(2), 193–218.
- Halliday, D. & Curtis, A., 2008. Seismic interferometry, surface waves and source distribution, *Geophysical Journal International*, **175**(3), 1067–1087.
- Hanasoge, S. M., 2013. The influence of noise sources on cross-correlation amplitudes, *Geophysical Journal International*, **192**(1), 295–309.
- Hanasoge, S. M., 2014. Measurements and kernels for source-structure inversions in noise tomography, *Geophysical Journal International*, **196**, 971–985.
- Kimman, W. P. & Trampert, J., 2010. Approximations in seismic interferometry and their effects on surface waves, *Geophysical Journal International*, **182**(1), 461–476.
- Li, G., Chen, H., Niu, F., Guo, Z., Yang, Y., & Xie, J., 2016. Measurement of Rayleigh wave ellipticity and its application to the joint inversion of high-resolution s wave velocity structure beneath northeast China, *Journal of Geophysical Research: Solid Earth*, **121**(2), 864–880.
- Lin, F.-C., Schmandt, B., & Tsai, V. C., 2012. Joint inversion of Rayleigh wave phase velocity and ellipticity using USArray: Constraining velocity and density structure in the upper crust, *Geophysical Research Letters*, **39**(12), L12303.
- Lin, F. C., Tsai, V. C., & Schmandt, B., 2014. 3-D crustal structure of the western United States: Application of Rayleigh-wave ellipticity extracted from noise cross-correlations, *Geophysical Journal International*, **198**(2), 656–670.
- Liu, Q., Koper, K. D., Burlacu, R., Ni, S., Wang, F., Zou, C., Wei, Y., Gal, M., & Reading, A. M., 2016. Source locations of teleseismic P, SV, and SH waves observed in microseisms recorded by a large aperture seismic array in China, *Earth and Planetary Science Letters*.
- Luo, Y., Yang, Y., Xu, Y., Xu, H., Zhao, K., & Wang, K., 2015. On the limitations of interstation distances in ambient noise tomography, *Geophysical Journal International*, **201**(2), 652–661.
- Maupin, V., 2017. 3-D sensitivity kernels of the Rayleigh wave ellipticity, *Geophysical Journal International*, **211**(1), 107–119.

- Muir, J. B. & Tsai, V. C., 2017. Rayleigh-Wave H/V via Noise Cross Correlation in Southern California, *Bulletin of the Seismological Society of America*, **107**(5), 2021–2027.
- Nakamura, Y., 1989. A METHOD FOR DYNAMIC CHARACTERISTICS ESTIMATION OF SUBSURFACE USING MICROTREMOR ON THE GROUND SURFACE, *Railway Technical Research Institute, Quarterly Reports*, **30**(1).
- Nakata, N., Chang, J. P., Lawrence, J. E., & Boué, P., 2015. Body wave extraction and tomography at Long Beach, California, with ambient-noise interferometry, *Journal of Geophysical Research: Solid Earth*, **120**(2), 1159–1173.
- Nakata, N., Boué, P., Brenguier, F., Roux, P., Ferrazzini, V., & Campillo, M., 2016. Body and surface wave reconstruction from seismic noise correlations between arrays at Piton de la Fournaise volcano, *Geophysical Research Letters*, **43**(3), 1047–1054.
- Pedersen, H. A. & Colombi, A., 2018. Body waves from a single source area observed in noise correlations at arrival times of reflections from the 410 discontinuity, *Geophysical Journal International*.
- Peterson, J. R., 1993. Observations and modeling of seismic background noise, USGS Numbered Series 93-322, U.S. Geological Survey, Code Number: 93-322 Code: Observations and modeling of seismic background noise Publication Title: Observations and modeling of seismic background noise Reporter: Observations and modeling of seismic background noise Series: Open-File Report.
- Poli, P., Pedersen, H. A., & Campillo, M., 2012. Emergence of body waves from cross-correlation of short period seismic noise, *Geophysical Journal International*, **188**(2), 549–558.
- Ringler, A. T., Wilson, D. C., Zürn, W., & Anthony, R. E., 2019. Rayleigh wave ellipticity measurement uncertainty across the IRIS/USGS and New China Digital Seismograph Networks, *Geophysical Journal International*, **217**(1), 219–237.
- Roux, P., 2009. Passive seismic imaging with directive ambient noise: application to surface waves and the San Andreas Fault in Parkfield, CA, *Geophysical Journal International*, **179**(1), 367–373.
- Roux, P., Sabra, K. G., Gerstoft, P., Kuperman, W. A., & Fehler, M. C., 2005. P-waves from cross-correlation of seismic noise, *Geophysical Research Letters*, **32**(19), L19303.
- Sager, K., Ermert, L., Boehm, C., & Fichtner, A., 2018. Towards full waveform ambient noise inversion, *Geophysical Journal International*, **212**(1), 566–590.

- Savage, M. K., Lin, F.-C., & Townend, J., 2013. Ambient noise cross-correlation observations of fundamental and higher-mode Rayleigh wave propagation governed by basement resonance, *Geophysical Research Letters*, **40**(14), 3556–3561.
- Saygin, E., Cummins, P. R., & Lumley, D., 2017. Retrieval of the P wave reflectivity response from autocorrelation of seismic noise: Jakarta Basin, Indonesia, *Geophysical Research Letters*, **44**(2).
- Shapiro, N. M. & Campillo, M., 2004. Emergence of broadband Rayleigh waves from correlations of the ambient seismic noise, *Geophysical Research Letters*, **31**(7), n/a–n/a.
- Snieder, R., 2004. Extracting the Green's function from the correlation of coda waves: A derivation based on stationary phase, *Physical Review E*, **69**(4), 046610, Publisher: American Physical Society.
- Stehly, L., Campillo, M., & Shapiro, N. M., 2006. A study of the seismic noise from its long-range correlation properties, *Journal of Geophysical Research*, **111**(B10), B10306.
- Tanimoto, T. & Rivera, L., 2008. The ZH ratio method for long-period seismic data: sensitivity kernels and observational techniques, *Geophysical Journal International*, **172**(1), 187–198.
- Tromp, J., Luo, Y., Hanasoge, S., & Peter, D., 2010. Noise cross-correlation sensitivity kernels, *Geophysical Journal International*, **183**(2), 791–819.
- Tsai, V. C., 2009. On establishing the accuracy of noise tomography travel-time measurements in a realistic medium, *Geophysical Journal International*, **178**(3), 1555–1564, Publisher: Oxford Academic.
- Tsai, V. C., 2011. Understanding the amplitudes of noise correlation measurements, *Journal of Geophysical Research*, **116**(B9), B09311.
- Wang, W., Gerstoft, P., & Wang, B., 2018. Seasonality of P wave microseisms from NCF-based beamforming using ChinArray, *Geophysical Journal International*, **213**(3), 1832–1848.
- Weaver, R. L. & Lobkis, O. I., 2004. Diffuse fields in open systems and the emergence of the Green's function (L), *The Journal of the Acoustical Society of America*, **116**(5), 2731–2734, Publisher: Acoustical Society of America.
- Xu, Z. & Mikesell, T. D., 2017. On the reliability of direct Rayleigh-wave estimation from multicomponent cross-correlations, *Geophysical Journal International*, **210**(3), 1388–1393.

- 459 Xu, Z., Mikesell, T. D., Gribler, G., & Mordret, A., 2019. Rayleigh-wave multicomponent cross-  
 460 correlation-based source strength distribution inversion. Part 1: Theory and numerical  
 461 examples, *Geophysical Journal International*, **218**(3), 1761–1780.
- 462 Yano, T., Tanimoto, T., & Rivera, L., 2009. The ZH ratio method for long-period seismic  
 463 data: inversion for \textlessi\textgreaterS\textless/i\textgreater-wave velocity structure,  
 464 *Geophysical Journal International*, **179**(1), 413–424.
- 465 Yao, H. & van der Hilst, R. D., 2009. Analysis of ambient noise energy distribution and phase  
 466 velocity bias in ambient noise tomography, with application to SE Tibet, *Geophysical*  
 467 *Journal International*, **179**(2), 1113–1132.

## Appendix

### A Model $M_0$

The model is shown in Table 1 and its surface wave eigen-solutions are plotted in Figures 6 and 7.

Table 1: The crustal model

Depth (Km)	$V_P$ (Km s <sup>-1</sup> )	$V_S$ (Km s <sup>-1</sup> )	$\rho$ (g cm <sup>-3</sup> )
0.00	6.200	3.600	2.800
17.00	6.600	3.700	2.900
34.00	7.300	4.000	3.100
50.00	8.200	4.700	3.400

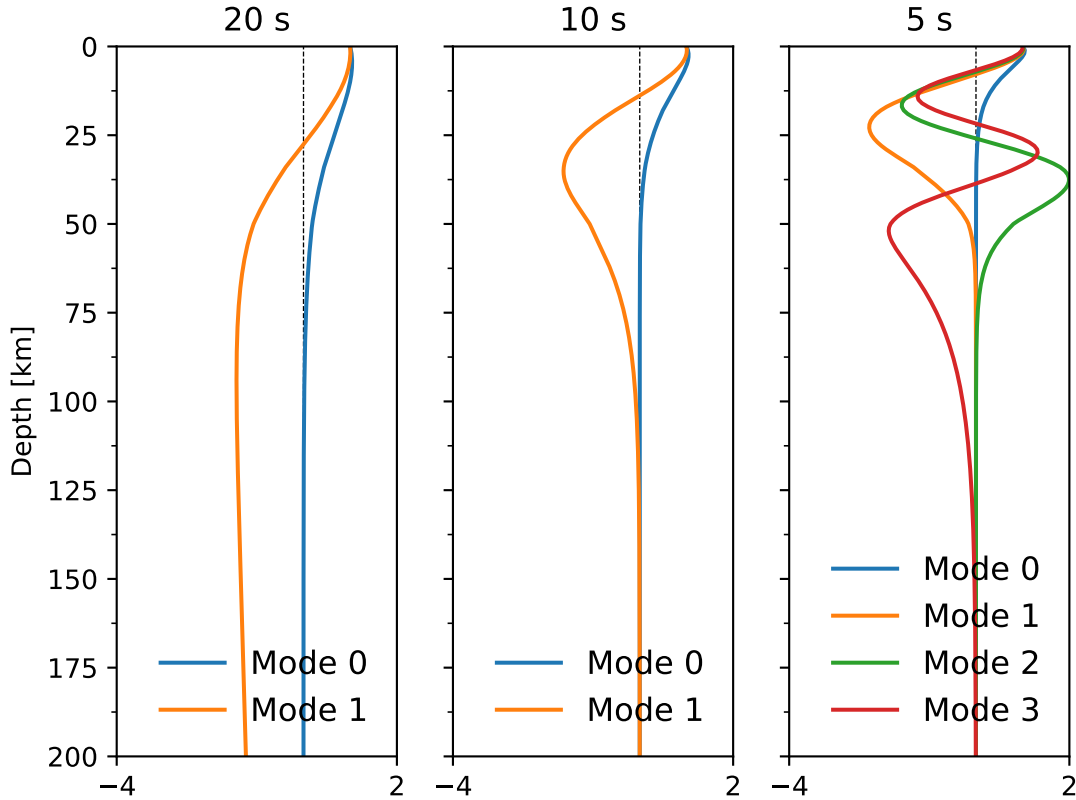


Figure 6: Rayleigh wave vertical displacement eigenfunctions (normalized to unit surface displacement) for the fundamental and higher modes in the model  $M_0$ , at three different periods indicated at the top. Note that most results in this paper are presented at 10 s period.

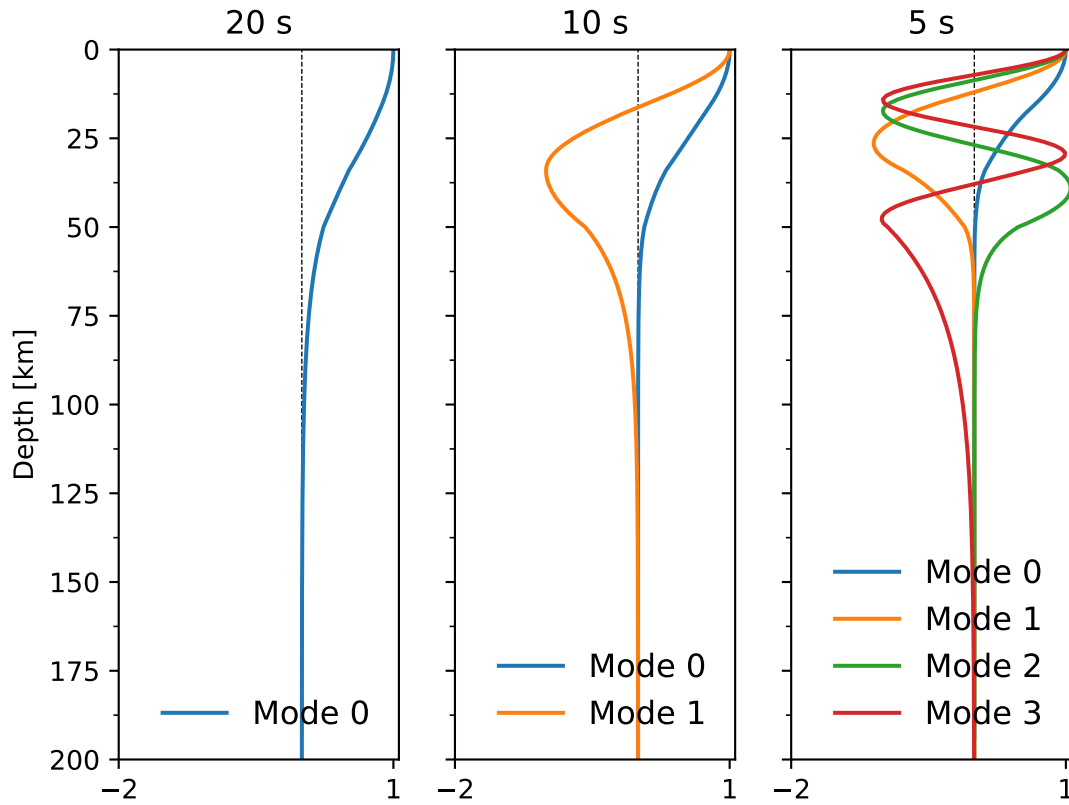


Figure 7: Love wave displacement eigenfunctions (normalized to unit surface displacement) for the fundamental and higher modes in the model  $M_0$ , at three different periods as in Figure 6.

472

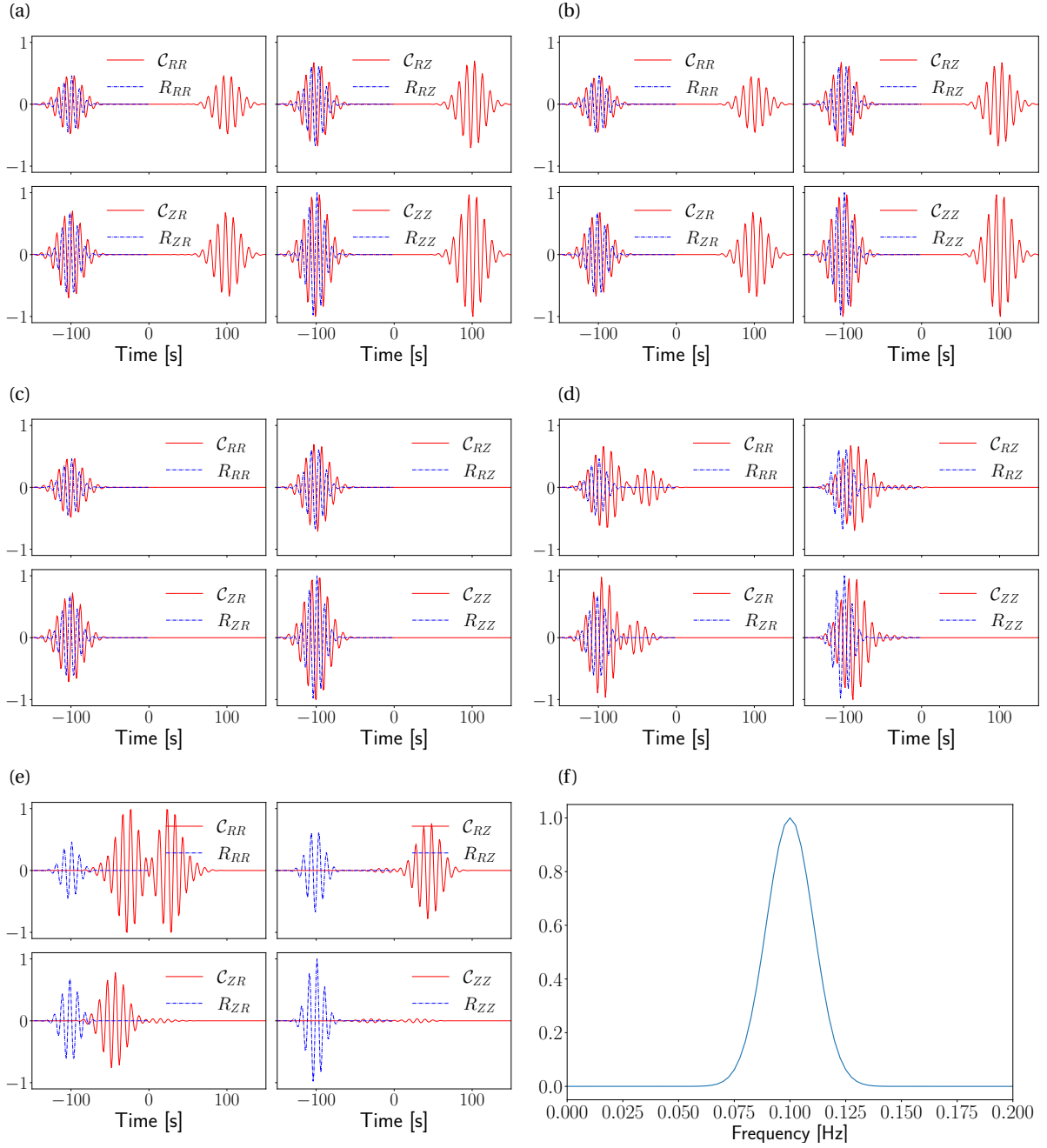
**B Supplementary Information**

Figure 8: Same as Figure 3 in the main text, but for 'xRL' source excitation.



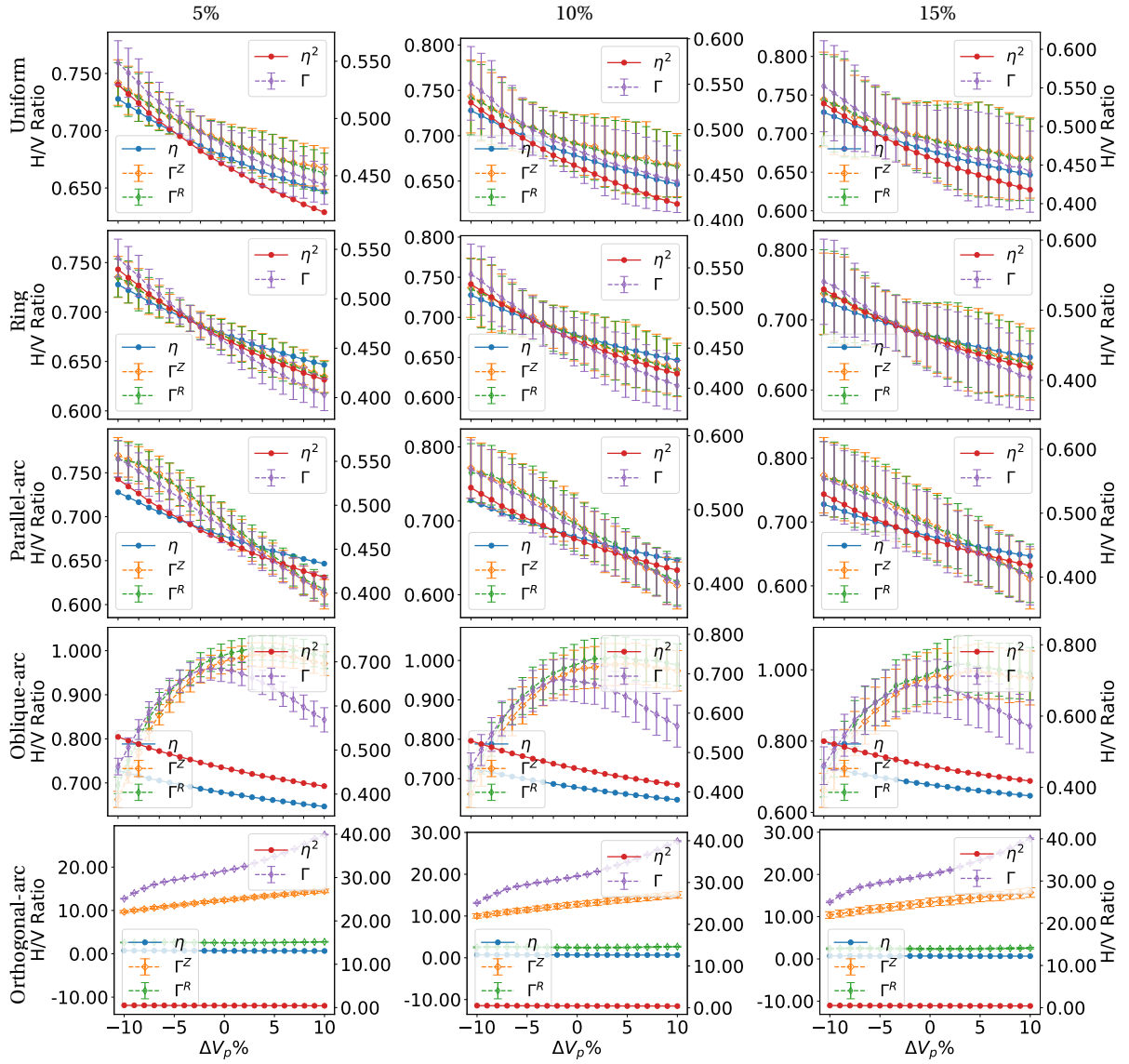


Figure 9: Same as Fig. 5 in the main text, but for 'xRL' source excitation.

For Frequency  $f = 0.1$  Hz.  
Layer perturbed

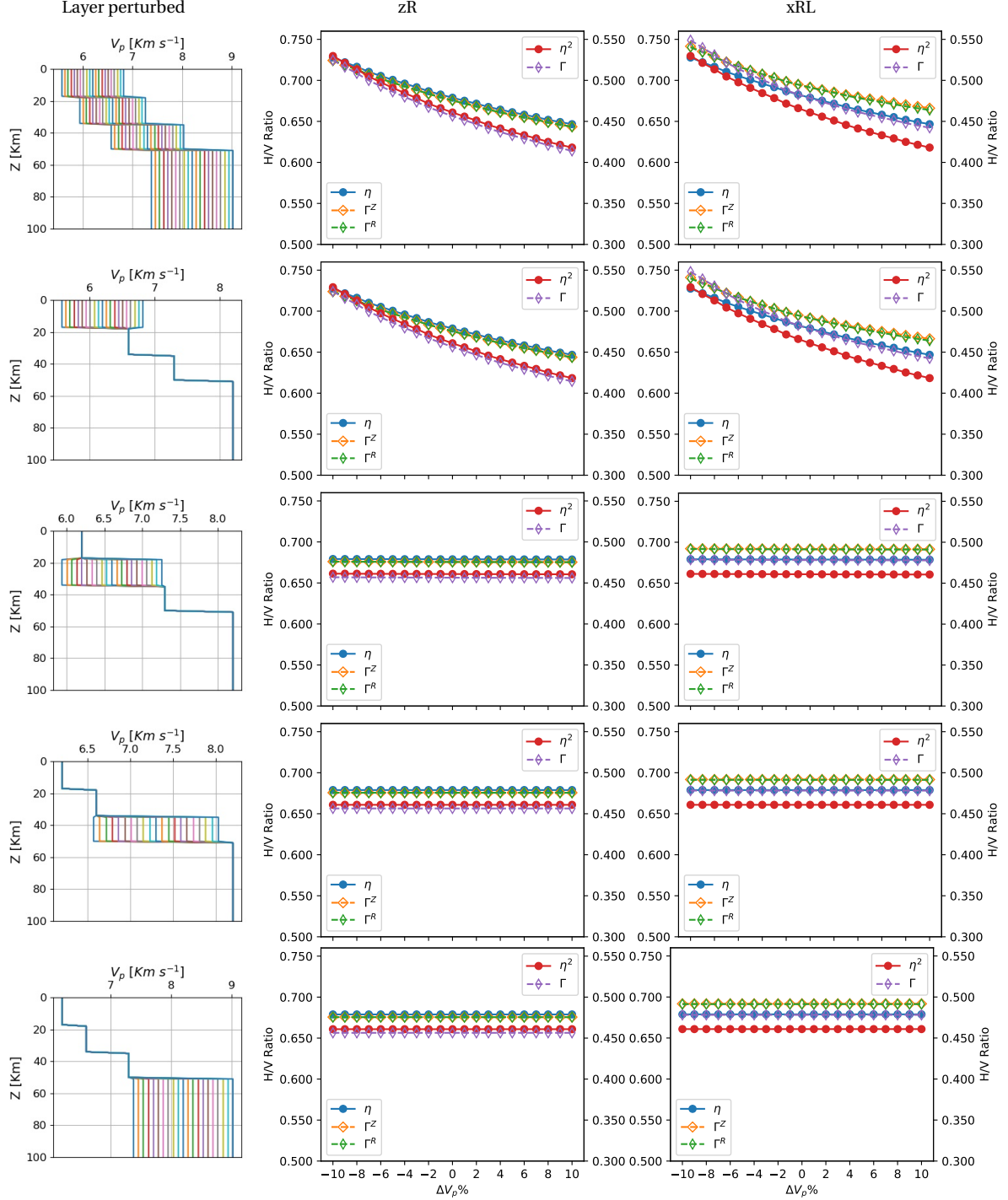


Figure 10: HVR sensitivity as a function of depth. Similar to Fig 4 but for a uniform source distribution and model perturbations applied at different depths as indicated on the left – all layers (same as Fig 4) in the top row, followed by layer-wise perturbation in each successive row. Note that the last ‘layer’ is the halfspace underlying the model.

For Frequency  $f = 0.75$  Hz.  
Layer perturbed

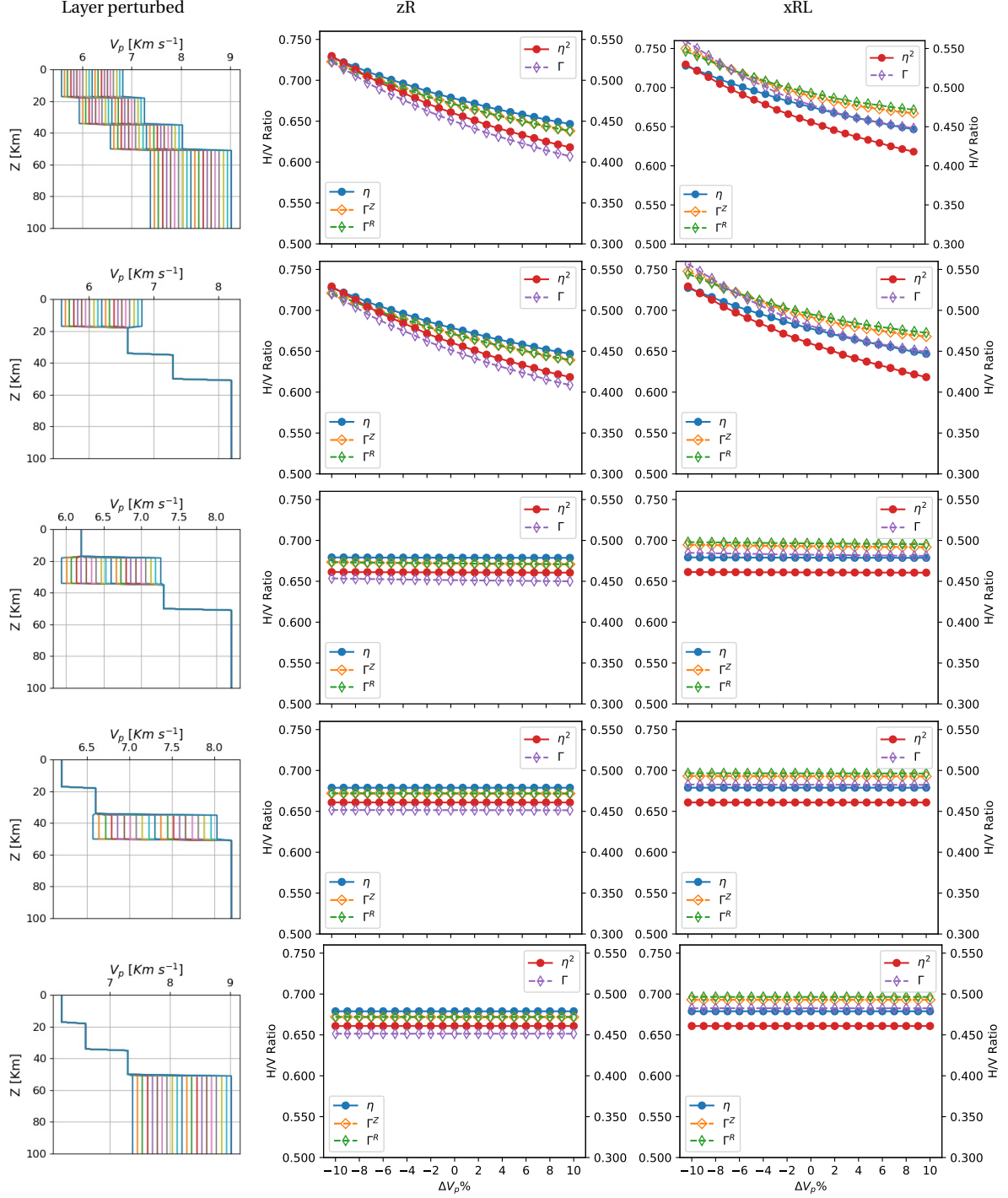


Figure 11: Same as Fig 10 but for  $f_0 = 0.75$  Hz, period  $\sim 13.33$  s.

For Frequency  $f = 0.05$  Hz.  
Layer perturbed

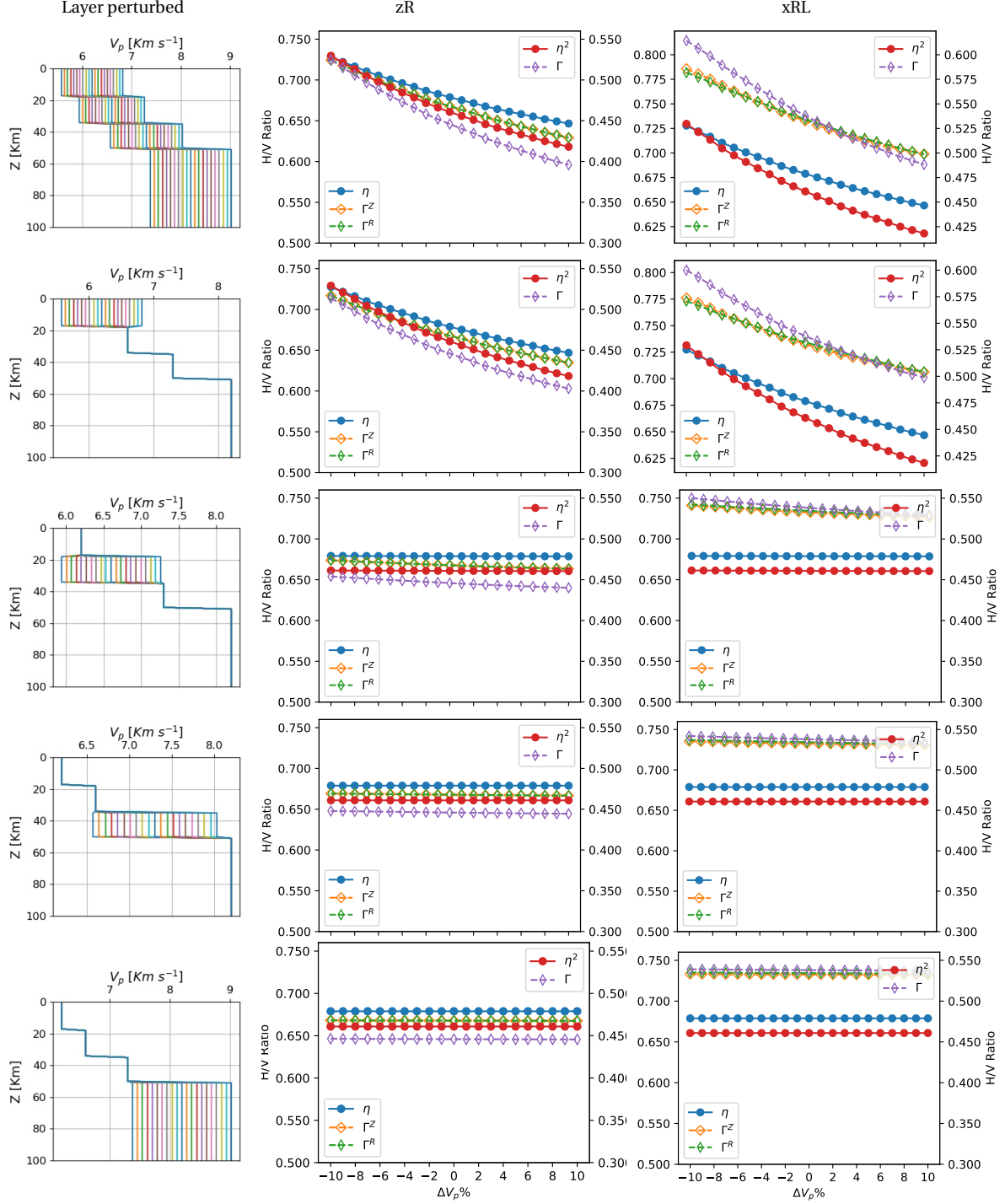


Figure 12: Same as Fig 10 but for  $f_0 = 0.05$  Hz, period 20 s.